IEEE Photonics Journal
An IEEE Photonics Society Publication

Three-Dimensional Measurement for Rigid Moving Objects Based on Multi-Fringe Projection

Volume 12, Number 4, August 2020

Jianhua Wang
Yanxi Yang
Mingwei Shao
Yuguo Zhou

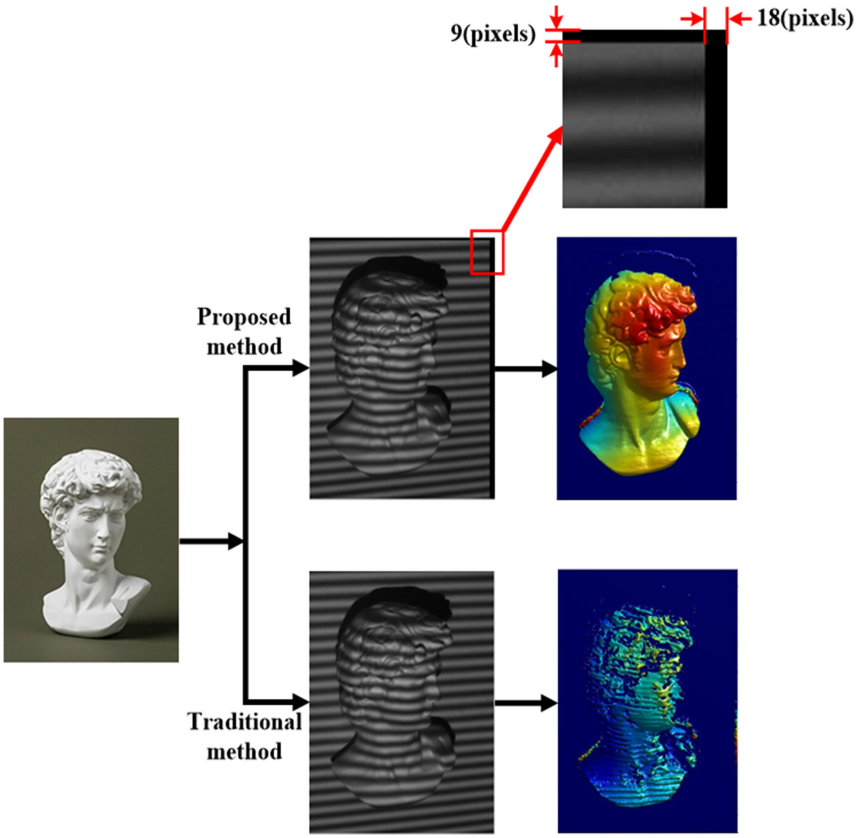

DOI: 10.1109/JPHOT.2020.3010545

Three-Dimensional Measurement for Rigid Moving Objects Based on Multi-Fringe Projection

Jianhua Wang,[1] **Yanxi Yang**,[2] **Mingwei Shao**,[1] **and Yuguo Zhou** [1]

[1]School of Information and Control Engineering, Qingdao University of Technology, Qingdao 266520, China
[2]School of Automation and Information Engineering, Xi'an University of Technology, Xi'an 710048, China

DOI:10.1109/JPHOT.2020.3010545

Manuscript received June 2, 2020; accepted July 15, 2020. Date of publication July 21, 2020; date of current version July 30, 2020. This work was supported by the Shaanxi Key Laboratory of Complex System Control and Intelligent Information Processing, Xi'an University of Technology. Corresponding author: Jianhua Wangwang (email: jianhua@qut.edu.cn).

Abstract: Multi-fringe projection profilometry, such as the widely used phase-shifting and temporal phase unwrapping algorithms, can achieve high accuracy and robustness in three-dimensional shape reconstruction of static objects. However, the motion of the objects will introduce errors. This paper proposes a new method to reconstruct 3D shape of rigid moving objects on an automated transmission line. First, a new pixel matching method for projected and captured images is proposed. Then, the pixel deviation caused by the motion of the objects in the three-dimensional direction is pre-detected, and the new projection fringes are obtained according to the above pixel matching. Third, the new projection fringes are binarized and the projector is defocused to realize high-speed projection. At last, the captured fringes are offset to reconstruct 3D shape. Experimental results show that the proposed method is effective in 3D shape reconstruction of rigid moving objects.

Index Terms: Phase-shifting, three-dimensional shape, pixel matching, pixel deviation.

1. Instruction

Fringe projection profilometry (FPP) has the characteristics of non-contact, high-precision, high-speed, low-cost and full-field measurement, which has been widely used in industrial detection, reverse engineering, cultural heritage preservation, bionic design, human body modeling and medical diagnosis, etc. [1]–[4]. Phase calculation is a key step in FPP, it can be divided into single fringe and multiple fringes projection and acquisition. The phase calculation accuracy and robustness of multiple fringes is higher, for example, a combination of the phase-shifting (PS) algorithm and the temporal phase unwrapping algorithm. However, it is not suitable for three-dimensional (3D) shape measurement of dynamic objects due to the multiple fringes projection and acquisition.

The dynamic objects can be divided into rigid moving objects and continuous deformation objects. This work focuses on 3D shape measurement of rigid moving objects, such as rigid moving objects on automated transmission line. At present, the commonly used method is to transport the measured objects to a 3D measurement system by a robot. After the 3D shape measurement is completed, the robot transports the measured objects back to the conveying line, which increases costs and reduces efficiency.

Many researchers have proposed a large number of 3D measurement methods for rigid moving objects. Generally, the accuracy and robustness of 3D measurement based on multiple fringes are higher. Here are some typical research results. Wang *et al.* [5] proposed a new phase unwrapping approach that combines the conventional spatial phase unwrapping algorithm with the gray code to solve the motion induced phase unwrapping problems. The gray code is first used to segment the whole image into separate regions. Within each region, the phase differences between neighboring pixels are no more than 2π. Then a conventional unwrapping algorithm is applied to unwrap the phase for each region to obtain relative phase. Finally, the gray code is again used to obtain absolute phase by properly shifting the relative phase for each region by adding multiples of 2π. By this means, the phase unwrapping problems caused by motion could be resolved. Lu *et al.* [6] proposed a new method to automatically measure the 3D shape of the rigid objects with arbitrary 2D movement. Firstly, the objects movement is tracked by the SIFT algorithm and the rotation matrix and translation vector describing the movement are estimated. Then, with the reconstruction model including movement information, a least-square algorithm is applied to retrieve the correct phase value. The proposed method can significantly reduce the errors caused by the objects movement. Feng *et al.* [7] present a novel motion-compensated phase-shifting profilometry (PSP) to remove the artifacts for dynamic measurements of rigid objects. The phase error of moving objects is analyzed for PSP and compensated using the statistical nature of the fringes. The phase unwrapping errors are corrected exploiting adjacent reliable pixels, and the outliers are removed by comparing the original phase map with a smoothed phase map. Compared with the three-step PSP, the method can improve the accuracy by more than 95% for objects in motion. Liu *et al.* [8] proposed a new method to reduce the phase errors introduced by motion based on PSP. Firstly, the motion of the object is estimated according to the difference between the two images. Then, using the pinhole model of the projector, the error caused by the motion is determined from the estimated motion. Finally, a new phase shift algorithm is used to calculate the phase. By compensating the phase shift error caused by rigid motion and non-rigid motion in FPP, it can realize the 3D measurement of rigid moving objects.

In this paper, we present a new method based on PS and three pitches heterodyne phase unwrapping (TPHPU) algorithms for rigid moving objects on automated transmission line. First, we discuss the errors caused by 3D linear motion of the rigid objects on automated transmission line. Then, we present a method to pro-detect pixel deviations of the captured fringes due to motion of the measured objects. Third, a new method of pixel matching between the projected and the captured images is proposed. Forth, new projected fringes are obtained according the adjusted capture images and pixel matching. Finally, we project the new fringes and capture them. The captured fringes are adjusted according to the pro-detect pixel deviations for 3D shape reconstruction. This approach inherits the high accuracy and robustness of the PS and TPHPU algorithms.

This paper is organized as follows. The principle of the proposed method is presented in Section 2. In Section 3, experimental results are given to verify the effectiveness of the proposed method. Section 4 summarizes this paper.

2. Principle

2.1 High-Precision Phase Calculation

PS and temporal phase unwrapping algorithms can achieve high accuracy and robustness in phase calculation. At least three phase-shifting fringe patterns are projected sequentially onto the object surface based on PS algorithm [9]–[11]. The ith fringe pattern can be expressed as

$$I_i(x, y) = A(x, y) + B(x, y)\cos[\phi(x, y) + 2\pi(i-1)/N] \tag{1}$$

where $A(x,y)$ is the average intensit, $B(x,y)$ is the intensity modulation, $\varphi(x,y)$ is the phase modulation of the fringes (the required phase distribution), i is a phase-shifting index and N is the total number of phase-shifting steps.

The wrapped phase based on PS algorithm can be expressed as

$$\psi(x, y) = \tan^{-1}\left\{\frac{-\sum_{i=1}^{N} I_i(x, y)\sin[2\pi(i-1)/N]}{\sum_{i=1}^{N} I_i(x, y)\cos[2\pi(i-1)/N]}\right\} \tag{2}$$

where $\psi(x, y)$ represents the wrapped phase. Due to the application of the $\tan^{-1}$ operator, $\psi(x, y)$ is between $-\pi$ and π taking into consideration of the real and imaginary parts.

There are three-step, four-step and five-step PS algorithms. Since three-step PSP has less fringes, it is adopted in this work.

$$\psi_{3-step}(x, y) = \tan^{-1}\left\{\frac{\sqrt{3}[I_1(x, y) - I_3(x, y)]}{2I_2(x, y) - I_1(x, y) - I_3(x, y)}\right\} \tag{3}$$

where $\psi_{3-step}(x, y)$ represents the wrapped phase calculated by three-step PS algorithm.

There are three typical temporal phase unwrapping methods, i. e. three pitches phase unwrapping (TPPU), TPHPU and negative exponential phase unwrapping (NEPU) methods [12], [13]. TPHPU has high efficiency while guaranteeing the higher reliability of the unwrapping phase.

Three frequencies of the projected fringes based on TPHPU are $f1 = K + \sqrt{K} + 1$ (K is a constant), $f2 = K$ and $f3 = K - \sqrt{K}$, respectively. First, the three-step phase-shifting algorithm is used to calculate the wrapped phases, i.e. $\psi^{K+\sqrt{K}+1}$, ψ^{K} and $\psi^{K-\sqrt{K}}$. Then, the wrapped phase of $\psi^{\sqrt{K}+1}$ is obtained from $\psi^{K+\sqrt{K}+1}$ and ψ^{K} employing the heterodyne method. Similarly, the wrapped phase of $\psi^{\sqrt{K}}$ is obtained from ψ^{K} and $\psi^{K-\sqrt{K}}$ employing the heterodyne method. Finally, $\psi 1$ is calculated from $\psi^{\sqrt{K}+1}$ and $\psi^{\sqrt{K}}$ employing the heterodyne method. Since $\varphi 1 = \psi 1$ (φ is unwrapped phase), the unwrapped phase with higher frequency (i. e. $\phi^{\sqrt{K}+1}$, $\phi^{\sqrt{K}}$, $\phi^{K+\sqrt{K}+1}$, ϕ^{K} and $\phi^{K-\sqrt{K}}$) can be obtained by using the following formula.

$$\begin{cases} \phi^{f_i}(x, y) = \psi^{f_i}(x, y) + R^{f_i}(x, y) \times 2\pi \\ R^{f_i}(x, y) = INT\left[\dfrac{(f_i/f_{(i-1)}) \times \phi^{f_{(i-1)}}(x, y) - \psi^{f_i}(x, y)}{2\pi}\right] \end{cases} \tag{4}$$

where f_i represents the frequency of the projected fringe, *INT* is a *round* operator.

Therefore, $\phi^{K+\sqrt{K}+1}$, ϕ^{K} or $\phi^{K-\sqrt{K}}$ can be regarded as the final unwrapped phase. In addition, for temporal phase unwrapping algorithms, the least square algorithm can be used to fit intermediate unwrapped phase information to obtain the fitting phase, which improves phase accuracy.

$$\phi^{f}(x, y) = f\frac{\sum_{i=1}^{3}\sum_{x=1}^{M}\sum_{y=1}^{N} f_i\phi^{f_i}(x, y)}{\sum_{i=1}^{3}(f_i)^2} \tag{5}$$

2.2 Analysis of Rigid Moving Objects on Automatic Transmission Line

For a rigid moving object, the feature point on the object at time t is $\mathbf{P_t} = [x_t, y_t, z_t]$, and this feature point at time $t+1$ is $\mathbf{P_{t+1}} = [x_{t+1}, y_{t+1}, z_{t+1}]$, then

$$\mathbf{P_t} = \mathbf{R}\mathbf{P_{t+1}} + \mathbf{T} \tag{6}$$

where $\mathbf{R}$ is rotation matrix, $\mathbf{T}$ is translation matrix.

If the measured object moves on an automated transmission line, the motion trajectory is generally a straight line in space and the motion speed is constant, as shown in Fig. 1. Then the formula (6) is simplified as

$$\mathbf{P_t} = \mathbf{P_{t+1}} + \mathbf{T} \tag{7}$$

According to Fig. 1, if three-step PS and TPHPU are employed to obtain the unwrapped phase information, the number of fringes is 9. When projecting and capturing 9 images, we require the measured object to be stationary. The characteristic point A of the measured object at time t

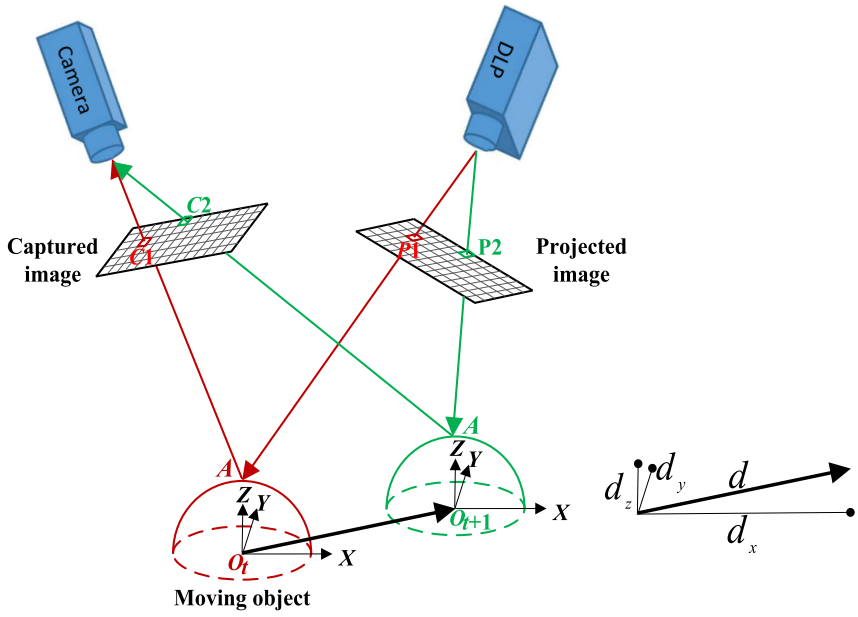

Fig. 1 Rigid moving object on an automatic transmission line.

corresponds to the pixel point P_1 of the projected image and the pixel point C_1 of the captured image. However, due to the motion of the object, the feature point A at time $t+1$ corresponds to the pixel point P_2 of the projected image and the pixel point C_2 of the captured image. The introduction of this error seriously reduces the accuracy of 3D shape reconstruction of a moving object based on three-step PS and TPHPU.

Assuming that the world coordinates are X, Y and Z. The displacement amount of a moving object in 3D space is d, as shown in Fig. 1. The motion components on the world coordinate system are d_X, d_Y and d_Z. The displacement deviation d_X in the X direction of the world coordinate system causes pixel deviations in the projected and captured images, as shown in Fig. 2. Assume that the pixel deviation of the projected image caused by d_X is P_X, and the pixel deviations in the height and width directions (projected image coordinate system) of the projected image are P_X^H and P_X^W. Similarly, assume that the pixel deviation of the captured image caused by d_X is C_X, and its pixel deviations in the height and width directions (captured image coordinate system) of the captured image are C_X^H and C_X^W. The displacement deviation d_Y in the Y direction of the world coordinate system causes the pixel deviations of the projected and captured images, as shown in Fig. 3. The pixel deviations on the projected image are P_Y^H and P_Y^W, and the pixel deviations on the captured image are C_Y^H and C_Y^W. The displacement deviation d_Z in the Z direction of the world coordinate system causes the pixel deviations of the projected and captured images, as shown in Fig. 4. The pixel deviations on the projected images are P_Z^H and P_Z^W, and the pixel deviations on the captured images are C_Z^H and C_Z^W.

$$\begin{cases} P^H = P_X^H + P_Y^H + P_Z^H \\ P^W = P_X^W + P_Y^W + P_Z^W \end{cases} \tag{8}$$

$$\begin{cases} C^H = C_X^H + C_Y^H + C_Z^H \\ C^W = C_X^W + C_Y^W + C_Z^W \end{cases} \tag{9}$$

Although many researchers have proposed a large number of solutions, we expect to propose a simpler and more effective method. Since the motion trajectory and speed are constant on the

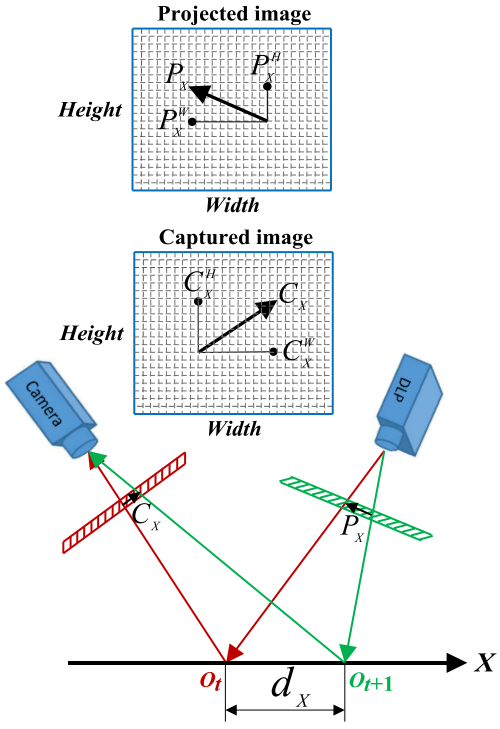

Fig. 2. The pixel deviations on the projected and captured images caused by d_X.

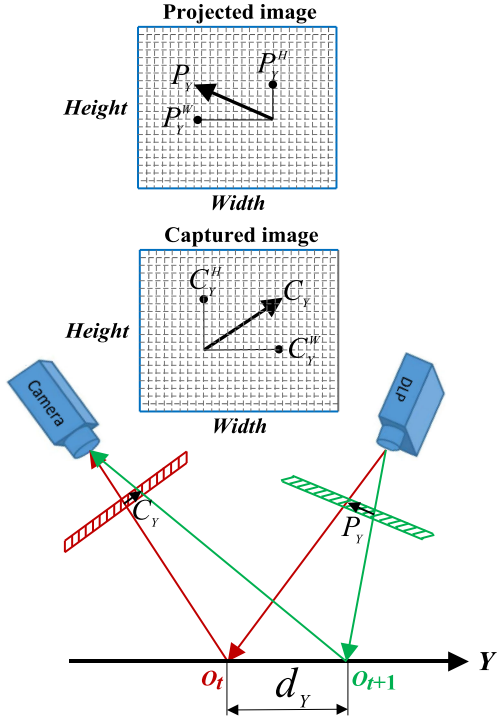

Fig. 3. The pixel deviations on the projected and captured images caused by d_Y.

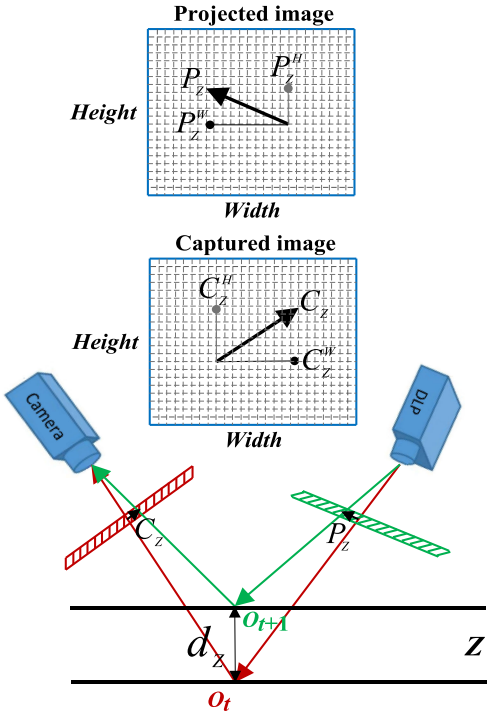

Fig. 4. The pixel deviations on the projected and captured images caused by d_Z.

automatic transmission line, we adopt the following four steps to achieve the spatial offset of 9 projected and captured images.

a) Calculate the pixel offset of the captured images caused by object movement, i. e. the acquisition of C_H and C_W in formula (9).
b) Pixel matching between the projected and captured images. Since the pixels of the projected and captured images do not match one by one, pixel matching is required.
c) New projected images are obtained according to (a) and (b).
d) The new projected fringes binarization and the projector defocus to achieve high-speed projection and capture.

2.3 Pixel Deviation Calculation of the Captured Image Caused by Moving Object

We place a black and white checkerboard on the automatic transmission line, as shown in Fig. 5. Corner pixel extraction algorithm is used to obtain pixel deviation between frames. In order to eliminate the occasional error, the average value of the pixel deviations between frames can be taken.

$$\begin{cases} C^H = \dfrac{\sum_{i=1}^{M}\left[C_t^H(i) - C_{t+1}^H(i)\right]}{M} \\ C^W = \dfrac{\sum_{i=1}^{M}\left[C_t^W(i) - C_{t+1}^W(i)\right]}{M} \end{cases} \tag{10}$$

where H and W represent the height and width directions of the capture image, i represents the ith corner point and M represents the total number of corner points.

The current corner detection algorithms can be summarized into three categories: corner detection based on gray images, corner detection based on binary images and corner detection based on contour curves. Here, corner detection based on gray images is used. Harris corner detection

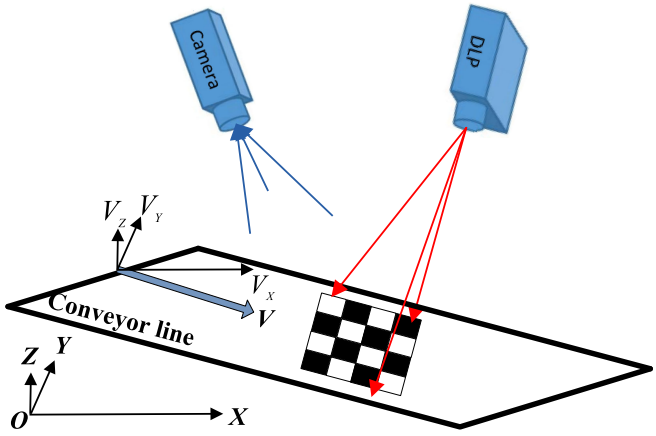

Fig. 5. Corner pixel extraction on the automatic transmission line.

is a typical method. The basic principle of Harris corner detection is to use a local window to move on the image and determine the gray level change in the window to identify the corner.

The grayscale change caused by the image window translation (u, v) is expressed as

$$E(u, v) = \sum_{x,y} w(x, y)[I(x + u, y + v) - I(x, y)]^2 \tag{11}$$

where $w(u, v)$ is window function, $I(x + u, y + v)$ is the gray value after translation, $I(x, y)$ is the gray value before translation.

Formula (11) is expanded by Taylor formula,

$$I(x + u, y + v) = I(x, y) + I_x u + I_y v + O(u^2 + v^2) \tag{12}$$

where I_x and I_y are the curvatures (partial differential) in the x and y directions, and O is the error term.

The grayscale change caused by the image window translation (u, v) can also be expressed as

$$E(u, v) = \sum_{x,y} w(x, y)[I_x u + I_y v + O(u^2 + v^2)]^2 \tag{13}$$

$$[I_x u + I_y v]^2 = \begin{bmatrix} u & v \end{bmatrix} \begin{bmatrix} I_x^2 & I_x I_y \\ I_x I_y & I_y^2 \end{bmatrix} \begin{bmatrix} u \\ v \end{bmatrix} \tag{14}$$

For a small amount of local displacement, the grayscale change is approximately expressed as

$$E(u, v) \cong \begin{bmatrix} u & v \end{bmatrix} \mathbf{M} \begin{bmatrix} u \\ v \end{bmatrix} \tag{15}$$

$$\mathbf{M} = \sum_{x,y} \begin{bmatrix} I_x^2 & I_x I_y \\ I_x I_y & I_y^2 \end{bmatrix} \tag{16}$$

Therefore, corner detection is equivalent to solving the eigenvalues of the matrix $\mathbf{M}$. Assume that the eigenvalues are λ_1 and λ_2, then

$\lambda_1 \to 0$ and $\lambda_2 \to 0$, there is no obvious gray change after the image window is moved.

$\lambda_1 \gg \lambda_2$ or $\lambda_2 \gg \lambda_1$, the edge is detected.

$\lambda_1 \gg 0$, $\lambda_2 \gg 0$ and the two eigenvalues are close, the corner point is detected.

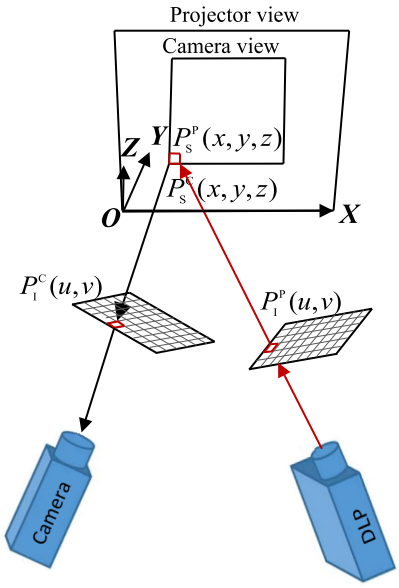

Fig. 6. The relationship between the projector view and the camera view.

2.4 Pixel Matching Method

If a pixel on the projected image is $P_I^P(u, v)$. When it is projected onto the reference plane, its spatial coordinate is expressed as $P_S^P(x, y, z)$.

$$K_P P_I^P = \mathbf{H}_{3\times4}^P P_S^P \tag{17}$$

where K_P is a coefficient, $\mathbf{H}_{3\times4}^P$ is a geometric transformation matrix with rotation and translation.

If a pixel on the camera's image is $P_I^C(u, v)$. Its corresponding spatial coordinate on the reference plane is expressed as $P_S^C(x, y, z)$.

$$K_c P_I^C = \mathbf{H}_{3\times4}^C P_S^C \tag{18}$$

where K_C is a coefficient, $\mathbf{H}_{3\times4}^C$ is a geometric transformation matrix with rotation and translation.

In this work, we adopt a simple and effective calibration method [14]. Using this method, the camera view is inside the projector view, as shown in Fig. 6. However, the projector view and the camera view are irregular due to the 3D measurement system. In addition, the position of the camera view in the projector view is also random. Therefore, it is hard to establish a relationship between $P_I^P(u, v)$ and $P_I^C(u, v)$.

We adopted a pixel matching method in this work [15]. The size of the projected image is 912 $\times$ 1140 pixels, and the size of the captured image is 1024 $\times$ 850 pixels. The principle of the pixel matching method is as follows.

a) We project an image in which the intensity of the middle row of the projected image (i.e. the intensity of the 570 row pixels of the projected image) is 1. As shown in Fig. 7, the intensity of the other pixels is 0. We capture the image and calculate the grayscale histogram. If there are two peaks in the grayscale histogram, the row of pixels with intensity 1 is in the field of view of the captured image. In contrast, if there is only one peaks in the grayscale histogram, the row of pixels with intensity 1 is out of camera view. In this work, the 570 row of pixels with intensity 1 is in the field of view of the captured image due to the 3D measurement system adjustment.

b) We project an image in which the intensity of the 569 row pixels of the projected image is 1 and calculate the grayscale histogram of the captured image. If the 569 row of pixels with intensity 1 is in the field of view of the captured image, it does not reached the upper limit,

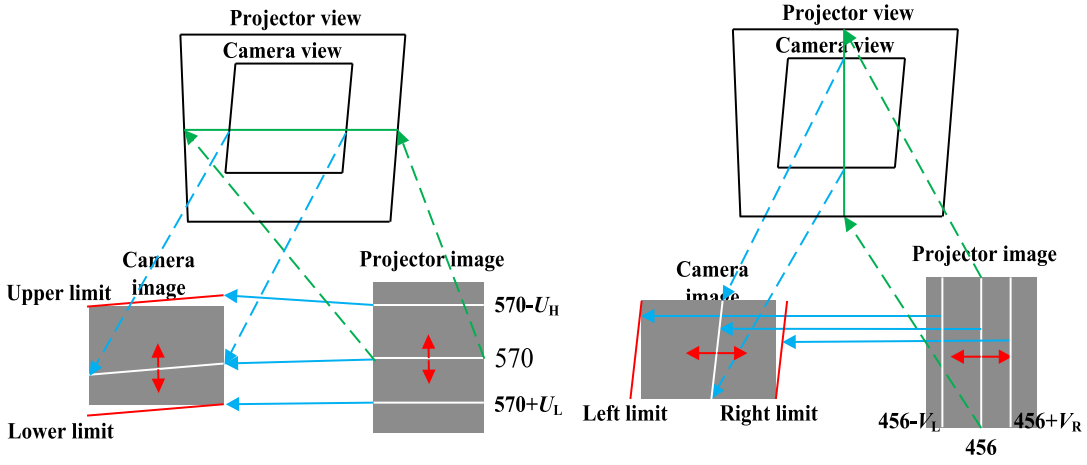

Fig. 7. Row and column scanning.

so the next image will continue to be projected. If the row of pixels with intensity 1 is out of camera view, the upper row can be found. According to the above method, the lower row can be found as well. Assume that the range of row and column numbers of the projected image are (570-U_H, 570+U_L) and (456-V_L, 456+V_R), respectively. U_H and U_L represent the row numbers of the upper and lower limit, V_L and V_R represent the column numbers of the lest and right limit.

c) The pixel matching between the projector image and the camera image. The pixel coordinate of the projector image that match the pixel coordinate (1, 1) in the camera image is

$$\begin{cases} P_{IR}^{C}(1,1) = \text{findrow}\left\{\max\left\{I_{570-U_H}(1,1),\ldots,I_{570+U_L}(1,1)\right\}\right\} \\ P_{IC}^{C}(1,1) = \text{findcolumn}\left\{\max\left\{I_{456-V_L}(1,1),\ldots,I_{456+V_R}(1,1)\right\}\right\} \end{cases} \tag{19}$$

where $P_{IR}^{C}(*,*)$ records the row number of the projector image that match the pixel coordinate ($*$, $*$) in the camera image, $P_{IC}^{C}(*,*)$ records the column number of the projector image that match the pixel coordinate ($*$, $*$) in the camera image, findrow is a row extraction operator, findcolumn is a column extraction operator, max is a maximum operator, $I_{570-U_H}(*,*)$ represents the grayscale of the pixel coordinate ($*$, $*$) of the captured image corresponding to the projected image in which the intensity of the (570-U_H) row pixels is 1, $I_{456-V_L}(*,*)$ represents the grayscale of the pixel coordinate ($*$, $*$) of the captured image corresponding to the projected image in which the intensity of the (456-V_L) column pixels is 1.

By using the above method, redundant images can be avoided. In addition, high-speed projection and acquisition can be combined to improve efficiency due to the binary images projection.

2.5 A method of Realizing High-Speed Projection

The refresh rate of cameras is high enough, however, the refresh rate of projectors is limited. For example, DLP LightCraft 4500 has a maximum refresh rate of 120 Hz for 8-bit image, but a maximum refresh rate of 4225 Hz for 1-bit image. There are three commonly used fringe binarization methods, i.e. square wave binarization method, SPWM binarization method and dithered binarization method. Dithered binarization method is further divided into Bayer dithered binarization method and dithered binarization method based on error diffusion. The authors have introduced the binarization methods in detail in Reference [16] and proved that the dithered binary based on error diffusion (DBED) is relatively better than the others.

The principle of DBED is to assign the error produced in the quantization process to a certain proportion of the pixels around it. First, fringe pattern with 256 levels of gray scale is normalized

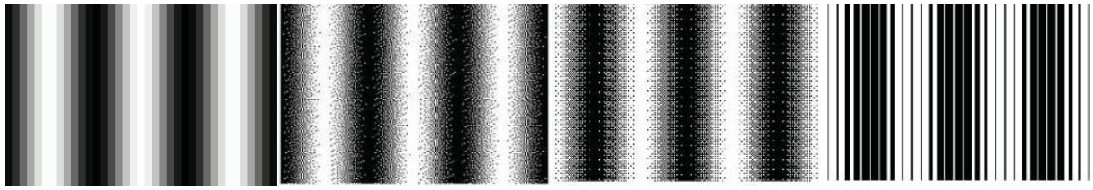

(a) (b) (c) (d)

Fig. 8. Fringe pattern: (a) 8-bit fringe pattern with cosine gray distribution, (b) 1-bit fringe pattern employing the dithered binarization method based on error diffusion, (c) 1-bit fringe pattern employing the Bayer dithered binarization method, and (d) 1-bit fringe pattern employing the SPWM binarization method.

and the image I is obtained; then a threshold T (such as $T = 0.5$) is set, and the binary fringe B is obtained. Finally, the error between I and B is calculated. By using a diffusion core, the error is assigned to the unprocessed pixels on the right, below, lower left, and lower right side. There are many kinds of diffusion cores, we choose the Floyd-Steinberg diffusion core here, the formula is

$$FS = \begin{bmatrix} - & * & \frac{7}{16} \\ \frac{3}{16} & \frac{5}{16} & \frac{1}{16} \end{bmatrix} \tag{20}$$

where symbols - is the left side pixel that do not require error allocation, symbols $*$ is the pixel being processed, the right pixel allocation error is 7/16, the lower left pixel distribution error is 3/16, the lower pixel distribution error is 5/16, and the right lower pixel distribution error is 1/16.

Fig. 8(a) shows a 8-bit fringe pattern with cosine gray distribution. Fig. 8(b) shows 1-bit fringe pattern employing the dithered binarization method based on error diffusion. Fig. 8(c) shows 1-bit fringe pattern employing the Bayer dithered binarization method. Fig. 8(d) shows 1-bit fringe pattern employing the SPWM binarization method. Dithered binarization method based on error diffusion is adopted in this work.

However, the binarization methods will introduce high-order harmonic components, resulting in phase calculation errors. The authors have introduced the defocusing technique of projector in detail in Reference [16].

The binarization fringe after the DLP defocusing can be expressed as

$$I_D(u, v) = I_B(u, v)G(u, v) \tag{21}$$

$$G(u, v) = \exp\left(-\frac{1}{2}(u^2 + v^2)\sigma^2\right) \tag{22}$$

where $I_D(x, y)$ is the binary fringe after projector defocusing in frequency domainin, $I_B(x, y)$ is the binary fringe in frequency domain, $G(u, v)$ is a Gauss function in frequency domain.

It is known from the characteristics of Gauss's function that the defocused optical system is equivalent to a low pass filter, which can filter out the high harmonic components, and the width of the filter is mainly determined by σ.

$$\sigma = \frac{kr}{2}s[v_1^{-1} - s^{-1}] \tag{23}$$

where k is scale coefficient which is greater than zero, r is the radius of the fuzzy circle, v_1 is the image distance, s is the distance from the fuzzy circle to the projector lens (i.e. the distance of the defocus).

According to the formula (23), we can see that σ is proportional to s. The bigger the defocus distance s is, the larger the σ, and the narrower the filter, the more high order harmonics of the filter. The smaller defocus distance s is, the smaller the σ, the wider the filter, the less high order harmonics of the filter [17].

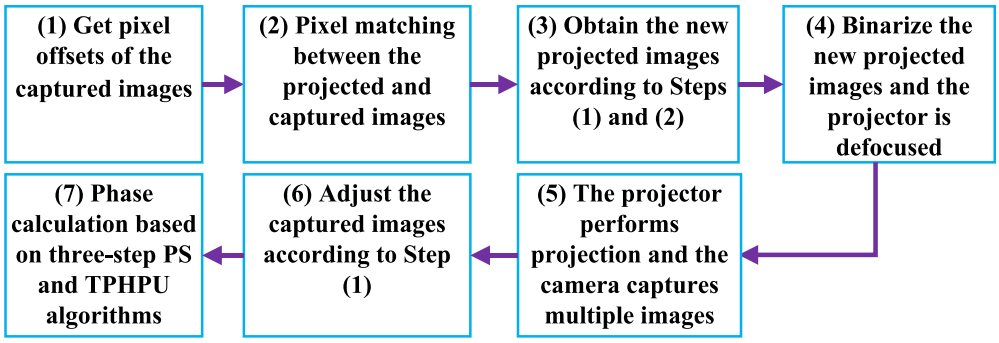

Fig. 9. Flow chart of the proposed method.

FFP calibration is done before the projector is defocused. When the projector and camera are fixed, we calibrate the 3D measurement system. Then we perform projector defocus. During 3D measurement process, we will project the binary images. After the images are defocused through the projector, the gray distribution is approximately sine or cosine distribution.

2.6 Procedure of the Proposed Method

Procedure the proposed method is described in Fig. 9.

Step 1: We get pixel offsets of the captured images according to Section 2. C. We place a black and white checkerboard on the motion transmission line in advance, and calculate the pixel offset of each captured image after extracting the checkerboard corners.
Step 2: We perform pixel matching of the projected and captured images according to Section 2. D. If the 3D measurement system is fixed, it can be pre-matched without any subsequent adjustments.
Step 3: We obtain the new projected images according to Steps (1) and (2).
Step 4: We get the binarized fringes according to Section 2. E, and then defocused the projector to reduce high-order harmonic components.
Step 5: The projector performs projection and the camera captures multiple images.
Step 6: We adjust the captured images according to Step 1.
Step 7: We obtain phase information according to Section 2. A.

3. Experiments

The structure of the 3D measurement system is shown in Fig. 10, including a DLP (DLP LightCraft 4500) from Texas Instruments, a camera (MER-131-210U3M) from Daheng Imaging and a personal computer (Intel Core i5-8265U, 8G RAM) from Lenovo. The projected images are stored in DLP. Computer reconstructs 3D shape after the processing of the captured fringes.

We place a David model on the automatic transmission line to verify the effectiveness of the proposed method, as shown in Fig. 11. Please note that, the motion trajectory is generally a straight line in 3D space and the motion speed is constant. The pixel matching method is adopted in advance, and no adjustment is required afterwards. Since three-step PS and TPHPU algorithms are used to calculate the phase information, the total number of fringe patterns is 9. The pixel offsets between the other fringe patterns (the second to ninth fringe pattern) and the first one can also be obtained employing the proposed method. So we can get 9 projected and captured fringe patterns after adjustment.

The pixel deviation between the last fringe pattern (the ninth fringe pattern) and the first one is the largest, so we give it in Fig. 11. The pixel deviations between the last fringe pattern and the first

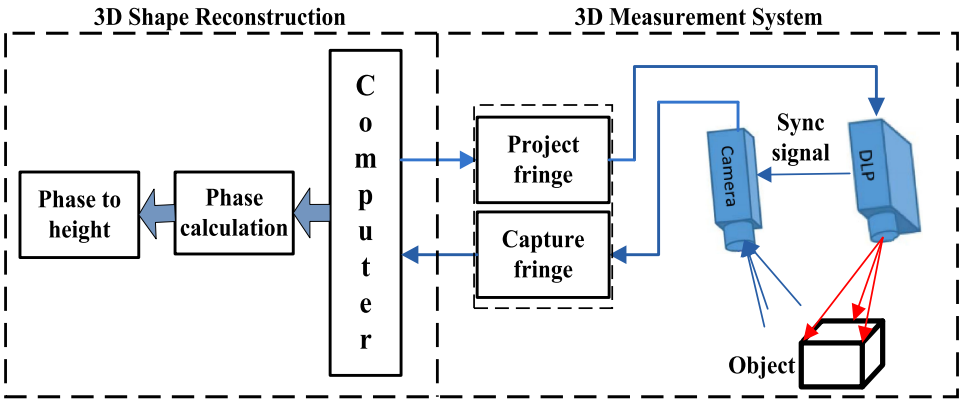

Fig. 10. Structure of the 3D measurement system.

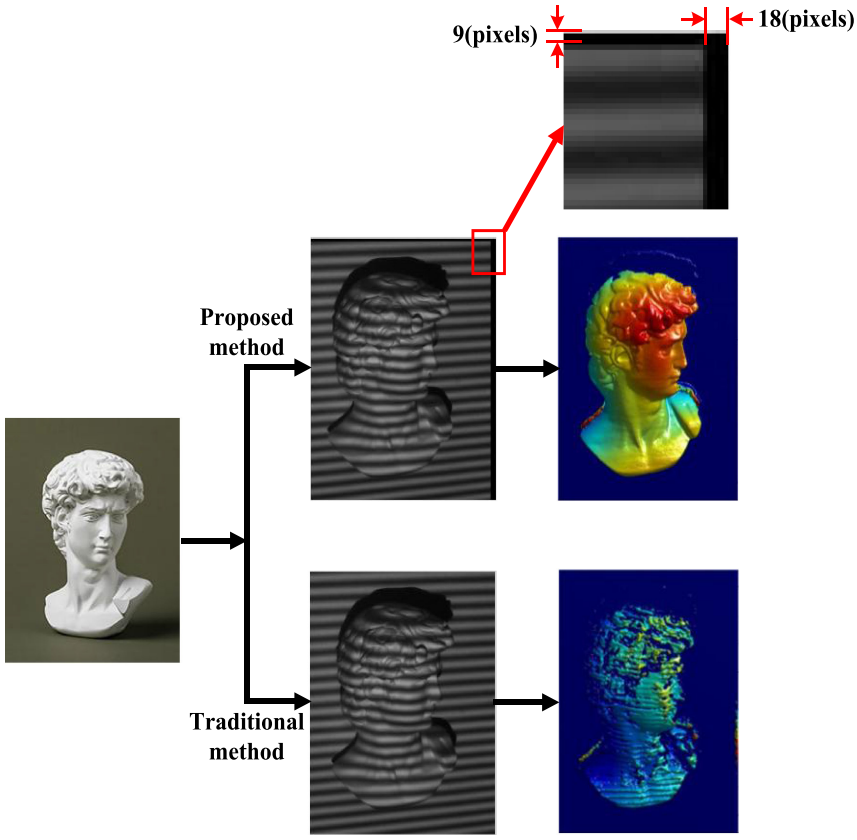

Fig. 11. Comparison of the reconstructed 3D shape on the automatic transmission line.

one in height and width direction are 9 and 18 pixels. The measured object is reconstructed with the traditional method and the proposed method, respectively. It can be seen that the reconstructed 3D shape based on the traditional method fails. However, the 3D reconstructed shape employing the proposed method is better, which verifies the effectiveness of the proposed method.

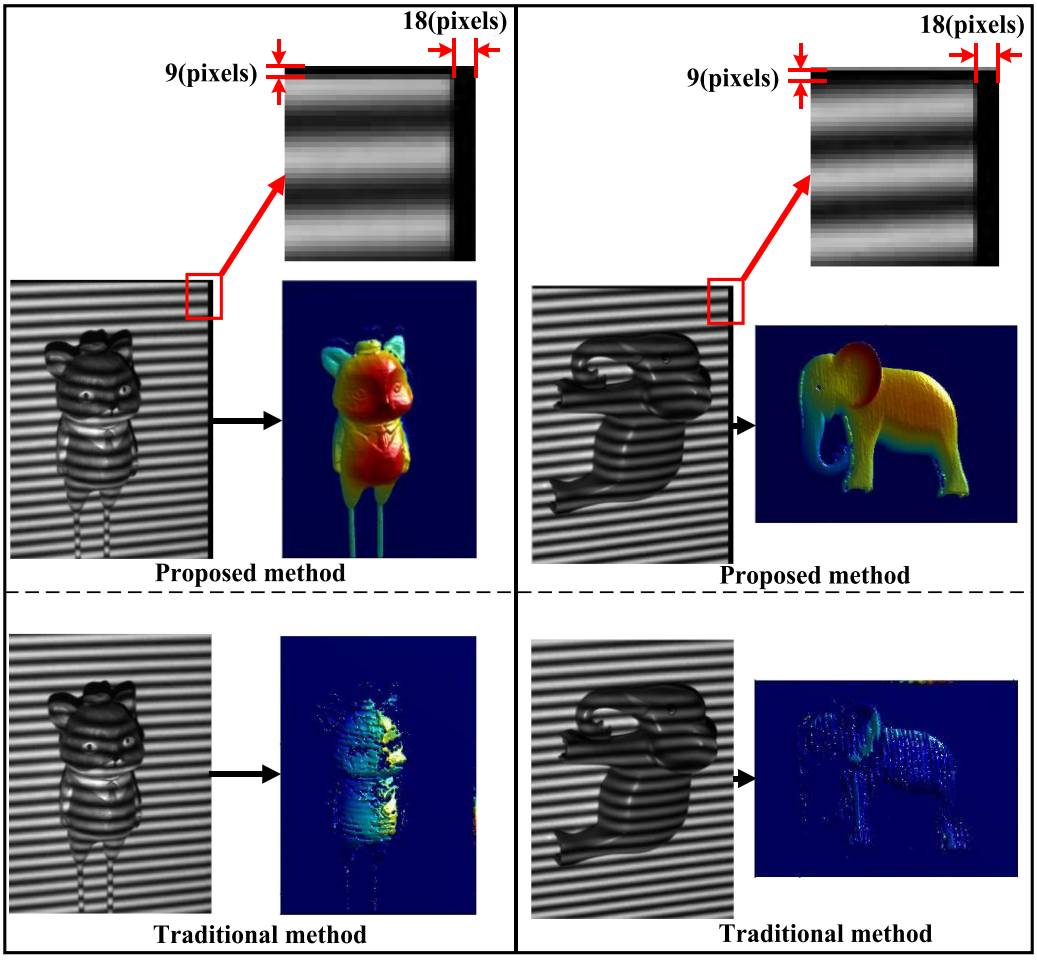

Fig. 12. Further comparison of the reconstructed 3D shape on the automatic transmission line.

To further verify the effectiveness of the proposed method, we take another two measured objects for comparison, as shown in Fig. 12. It is apparent that significant errors are introduced based on the traditional method, the 3D reconstructed shape employing the proposed method is good.

4. Conclusion

In this paper, we proposed a new method to reconstruct the 3D shape of rigid moving objects. This method preprocesses the fringe patterns of moving objects in 3D space, instead of complex phase compensation. The captured fringes are similar to that of static objects, so it inherits the high accuracy and robustness of PS and TPHPU algorithms.

Although this method has two manual operations in advance, there is no need to operate in the future after one manual intervention. The first manual intervention is to get the pixel deviation of the captured image caused by the motion in advance. For the rigid moving objects with certain trajectory and stable motion, such as the rigid moving objects on an automatic transmission line, only one manual operation is needed in advance, and no adjustment is needed in the future. The second manual intervention is to get the pixel matching between the projected and captured images. When the projector and camera in the 3D measurement system are relatively fixed, the

pixel matching between the projected and captured images only needs to be calibrated once, and there is no need to adjust in the future as well.

Experimental results show that the method is effective. It should be noted that this method only deals with rigid objects moving in a certain, predicable, steady state of motion. Therefore, it shows promise for helping to develop a 3D measurement device for rigid moving objects on an automated transmission line with high accuracy.

Disclosures

The authors declare no conflicts of interest.

References

[1] S. Zhang, "High-speed 3D shape measurement with structured light methods: A review," *Opt. Lasers Eng.*, vol. 106, pp. 119–131, Jul. 2018.
[2] Z. J. Wu, W. B. Guo, and Q. C. Zhang, "High-speed three-dimensional shape measurement based on shifting Gray-code light," *Opt. Express*, vol. 27, no. 16, pp. 22631–22644, Aug. 2019.
[3] W. Zhang, L. D. Yu, W. S. Li, H. J. Xia, H. X. Deng, and J. Zhang, "Black-box phase error compensation for digital phase-shifting profilomtry," *IEEE Trans. Instrum. Meas.*, vol. 66, no. 10, pp. 2755–2761, Oct. 2017.
[4] M. H. Duan, Y. Jin, C. M. XU, X. B. Xu, C. A. Zhu, and E. H. Chen, "Phase-shifting profilometry for the robust 3-D shape measurement of moving objects," *Opt. Express*, vol. 27, no. 16, pp. 22100–22115, Aug. 2019.
[5] Y. J. Wang, S. Zhang, and J. H. Oliver, "3D shape measurement technique for multiple rapidly moving objects," *Opt. Express*, vol. 19, no. 9, pp. 8539–8545, Apr. 2011.
[6] L. Lu, Y. Ding, Y. S. Luan, Y. K. Yin, Q. Liu, and J. T. Xi, "Automated approach for the surface profile measurement of moving objects based on PSP," *Opt. Express*, vol. 25, no. 25, pp. 32120–32131, Nov. 2017.
[7] S. J. Feng *et al.*, "Robust dynamic 3-D measurements with motion-compensated phase-shifting profilometry," *Opt. Lasers Eng.*, vol. 103, pp. 127–138, Dec. 2017.
[8] Z. P. Liu, P. C. Zibley, and S. Zhang, "Motion-induced error compensation for phase shifting profilometry," *Opt. Express*, vol. 26, no. 10, pp. 12632–12637, May. 2018.
[9] Y. Xing, C. Quan, and C. J. Tay, "A generalized multi-sensitivity temporal phase unwrapping method for absolute phase retrieval," *Opt. Laser Technol.*, vol. 96, pp. 290–298, Nov. 2017.
[10] T. Y. Tao, Q. Chen, J. Da, S. J. Feng, Y. Hu, and C. Zuo, "Real-time 3D shape measurement with composite phase-shifting fringes and multi-view system," *Opt. Express*, vol. 24, no. 18, pp. 20253–20269, Sep. 2016.
[11] S. J. Feng *et al.*, "Robust dynamic 3D measurements with motion-compensated phase-shifting profilometry," *Opt. Lasers Eng.*, vol. 103, pp. 127–138, Apr. 2018.
[12] C. Zuo, L. Huang, M. L. Zhang, Q. Chen, and A. Asundi, "Temporal phase unwrapping algorithms for fringe projection profilometry: A comparative review," *Opt. Lasers Eng.*, vol. 85, pp. 84–103, Oct. 2016.
[13] S. Xing and H. Guo, "Temporal phase unwrapping algorithms for fringe projection profilometry aided by recursion of Chebyshev polynomials," *Appl. Opt.*, vol. 56, no. 6, pp. 1591–1602, Feb. 2017.
[14] D. An, F. Da, S. Gai, and Ke Lu, "New system calibration method based on fringe projection profilometry," *J. Appl. Opt.*, vol. 35, no. 1, pp. 81–84, 2014.
[15] J. H. Wang, Y. G. Zhou, and Y. X. Yang, "Three-dimensional measurement method for nonuniform reflective objects," *IEEE Trans. Instrum. Meas.*, to be published, doi: 10.1109/TIM.2020.3001413.
[16] J. H. Wang and Y. X. Yang, "High-speed three-dimensional measurement technique for object surface with a large range of reflectivity variations," *Appl. Opt.*, vol. 57, no. 30, pp. 9172–9182, Oct. 2018.
[17] S. Zhang, "Flexible 3-D shape measurement using projector defocusing," *Opt. Lett.*, vol. 34, no. 20, pp. 3080–3082, Oct. 2009.